Hydrothermal Physics Based Modelling and Safety Constrained Multi Objective Seismic Design of Fluid Viscous Dampers

Haşmet Çağrı SEZGEN[a,*]

[a]*Mechanical Engineering Department, Necmettin Erbakan University, KONYA, Türkiye*

Abstract

Recent earthquakes show that some buildings with code compliant design and fluid viscous dampers (FVDs) still develop large interstorey drifts and floor accelerations in rare, high intensity events. A reason is that design models often reduce FVDs to black box power law dashpots, so internal pressure, cavitation and temperature never appear as explicit constraints. We address this by coupling a hydro thermal FVD model to a ten storey shear frame and optimising damper properties for both structural demand and device scale safety. The model captures laminar and jet branches, cavitation and temperature dependent oil properties through a Reynolds dependent discharge coefficient and a two node thermal block that feeds back into viscosity. We embed this device in time history analyses of the frame under ten ground motions, scaled to a spectral acceleration band centred on the first mode period. All response and safety metrics are evaluated on the 5-95% Arias intensity window. A multi parameter design space is then explored with NSGA II. Quality control thresholds on pressure, flow capacity ratio, cavitation, temperature and viscosity are enforced before trading off mean roof peak floor acceleration (PFA) and maximum interstorey drift ratio (IDR). The selected knee point on the Pareto front reduces the mean roof PFA from 13.27 to 5.05 m/s^2 and the mean maximum IDR from 0.88% to 0.30%, while satisfying all safety limits. An energy balance indicates that the orifice branch dissipates about 3.5×10^7 J versus 2.2×10^7 J in the structural viscous branch. In this configuration, most seismic input is converted to heat in the devices. Taken

---

*Corresponding author.

Email address: hasmetcagri.sezgen@erbakan.edu.tr (Haşmet Çağrı SEZGEN)

together, these results bring damper scale hydro thermal physics into safety first, performance based design for code oriented building archetypes.

---

1. Introduction

Many code compliant buildings still experience large interstorey drifts and floor accelerations during rare but intense earthquakes. Despite the shift from simple strength checks to performance based design, serviceability related demands in high seismic regions remain difficult to control. In practice, some frames satisfy global strength and code level ductility checks and still develop interstorey drift ratios (IDR) large enough to crack non structural components and architectural finishes. At the same time, peak floor accelerations (PFA) increase the fragility of suspended ceilings, façades, contents and sensitive equipment. When large IDR and high PFA occur together, they can trigger disproportionate economic and functional losses. To control these demands without resorting to very stiff or heavily over strengthened lateral systems, engineers increasingly rely on supplemental damping devices. Examples include metallic yielding dampers, friction devices, tuned mass dampers, base isolation systems and, in particular, velocity dependent fluid viscous dampers (FVDs), which are widely used in buildings and bridges as passive energy dissipation devices [62, 24, 60]. Major design codes such as EN 15129 and ASCE 7 explicitly recognise FVDs and provide guidance on their use in seismic applications [48, 7]. In most design procedures, these devices are represented through equivalent viscous damping and a power law force velocity relation of the form

$$F = C|v|^{\alpha},$$

where the pair (C, α) is calibrated from qualification tests. The same constants are then embedded in equivalent single degree of freedom (SDOF) or low order multi degree of freedom models for time history analysis [11, 35]. Several studies report that nonlinear FVDs with $\alpha < 1$ can achieve drift reductions comparable to those of linear devices, but with smaller damper forces and connection demands [19, 36, 20]. Life cycle and reliability based frameworks indicate that well tuned nonlinear viscous dampers (NFVDs) can reduce expected losses even when they involve a modest increase in initial device cost [9, 61, 8]. Placement and configuration studies show that the efficiency of a

1

given damper budget depends strongly on floor wise allocation and device type, with high performing layouts often concentrating capacity in selected storeys rather than spreading it uniformly [11, 33, 23]. Overall, these studies have established FVDs as a standard tool for performance based design of buildings and bridges, yet most formulations still treat the device as a black box dashpot governed by a small set of constant parameters.

Analytical and design oriented studies usually start from a phenomenological power law element of the form

$$F_{\mathrm{vd}} = C \, |\dot{u}|^{\alpha} \, \mathrm{sgn}(\dot{u}),$$

sometimes combined with simple floor wise placement rules for linear or nonlinear devices [36, 11, 19, 8, 62]. This representation is attractive because it involves only a few parameters, can be identified directly from full scale hysteresis loops and fits naturally into nonlinear response history analysis. A second line of models replaces the pure dashpot by a Maxwell type combination of a nonlinear dashpot and an axial spring, or by an equivalent complex stiffness in the frequency domain [6, 21]. These formulations capture frequency dependent stiffness and the inflated force velocity loops observed in large scale tests more accurately than a memoryless dashpot. In nonlinear time integration schemes they also keep numerical errors at acceptable levels. A third family introduces explicit hysteresis through Bouc-Wen type or related differential laws, including specialised formulations proposed for fluid viscous dampers [15, 20, 36]. These models have been tuned to reproduce pinching, strength degradation and specimen to specimen scatter within a single parameter set. Across all three families, calibration relies almost entirely on global F–u or F–$\dot{u}$ loops. Internal pressure, flow capacity, cavitation onset and temperature driven viscosity loss do not appear explicitly in the state variables or in the constraints of the design problem. Checks on these device scale quantities are rare in the modelling literature and, when reported, are usually confined to separate qualification tests on a small number of prototypes under almost isothermal, short duration loading [52, 62].

In parallel, several recent studies have started to examine the internal physics of fluid viscous dampers in more detail. These studies examine the thermal and hydraulic processes that lie behind simple

$$F = C|\dot{u}|^{\alpha}$$

laws. Early theoretical studies by Black and Makris suggested that, under highly idealised long duration pulses, internal oil temperatures could rise

2

well above 200 °C with a corresponding loss of damping capacity [10]. More recent full scale self heating experiments have largely corrected this picture for building type demands. For a typical commercial device, Laka and Zahrai report that earthquake like histories heat the housing by only about 2 to 3 °C, whereas long or highly cycled harmonic protocols can drive the temperature increase up to about 50 °C and noticeably weaken the force velocity response [37]. In a series of gap type damper tests combined with thermal and mechanical modelling, Zhang et al. [60] observed internal pressures of about 10^2 MPa for the most severe loading protocol. For the same protocol, local oil temperatures approached or slightly exceeded 200 °C. In these regimes, the dynamic viscosity dropped by roughly one order of magnitude and the peak force degraded by about 20% over a single long test [60]. On the modelling side, high fidelity CFD studies with coupled flow and heat transfer resolve laminar and jet branches and track the associated Reynolds dependent discharge coefficients [24, 4, 61]. Many of these simulations use Carreau-Yasuda rheology together with compressible flow laws and pressure- and temperature-dependent oil properties. Together, these contributions indicate that the effective (C, α) pair is strongly influenced by geometry, rheology and temperature. They also indicate that laminar gap flow, jet orifice losses, cavitation and heat transfer govern the internal histories of pressure, flow and temperature. They also emphasise that device integrity is governed by limits on pressure and temperature at seals and cylinders [29, 62]. Neglecting coupled hydraulic and thermal effects can bias the inferred supplemental damping ratio in multi degree of freedom analyses by about 10 to 12% [29]. However, almost all of these studies remain at specimen scale, or at most consider a single prototype structure under a handful of sinusoidal or recorded excitations. When FVDs are embedded in building or bridge models, the devices are usually collapsed back to isothermal phenomenological elements and only structural metrics such as interstorey drift, peak floor acceleration or damage indices are tracked [35, 11, 9, 8].

At structural level, numerous studies have optimised FVD parameters and placement with respect to drift, acceleration and economic losses under sets of ground motions. Examples include differential evolution or genetic algorithm based allocation of constant C devices along the height of shear buildings [11, 33], stochastic or energy based tuning of NFVD parameters via equivalent linearisation [20], and multi objective or semi active designs in which NSGA II or related algorithms trade off IDR and PFA under multiple records [9, 20]. Life cycle and reliability based frameworks embed FVD properties into risk

3

or cost functionals, and they generally report that well placed dampers can reduce expected annual loss and total life cycle cost [35, 9, 61, 8]. Some studies also find that NFVD parameters can be chosen to satisfy target reliabilities with lower steel tonnage and device cost than conservative code based designs [35, 9]. Applications to frames with soil structure interaction, cable stayed and highway bridges, and experimental shake table studies underline that damper effectiveness depends on structural configuration, soil profile, layout and damper technology [62, 33, 23]. These works also suggest that a single equivalent damping ratio is often inadequate to summarise behaviour across intensity levels. Despite this breadth, almost all of the above frameworks still represent the damper by an isothermal phenomenological or Maxwell type element and include only structural response or risk measures (interstorey drift ratios, peak floor accelerations, damage indices, annual loss) in the objective functions and constraints. Internal pressure, flow capacity, cavitation and temperature are not tracked or enforced explicitly within the optimisation loop.

In this context, the present paper proposes a safety driven design framework for FVD equipped shear buildings that links device scale physics with multi record, performance based seismic assessment. First, we develop an ODE-only fluid viscous damper model that separates laminar gap and orifice jet branches and assigns a Reynolds-dependent discharge coefficient with a soft minimum cavitation limiter. The same model also couples a two-node thermal block to temperature-dependent viscosity and density. This model tracks pressure, flow and temperature histories consistently while the damper is embedded in the equations of motion of a ten degree of freedom shear frame. In contrast to detailed CFD simulations conducted at specimen level [4, 37, 24, 61], it is deliberately kept inexpensive enough for large ground motion sets. Second, we adopt a band averaged geometric mean spectral acceleration centred at the first mode period as intensity measure. We evaluate both structural and device metrics within a common Arias window $[t_5, t_{95}]$, including peak floor accelerations, interstorey drifts, pressure percentiles, Q/Q_{cap}, cavitation ratio, end of record temperature and viscosity, thereby extending Sa,avg type intensity measures and significant duration concepts to a joint assessment of building performance and internal damper safety [54, 17, 29]. Third, we cast the FVD design problem as a lexicographic multi objective optimisation in a twelve dimensional space of orifice geometry, piston and spring parameters and thermal properties. We first minimise an aggregated penalty f_{pen} that counts hydraulic and thermal quality control

4

violations (pressure capacity, flow throttling, cavitation onset, temperature and viscosity limits). Only designs with low f_{pen} are then used to trade off average peak floor accelerations and interstorey drifts via NSGA II. This safety first formulation goes beyond existing multi objective or risk informed designs that tune simple power law or Maxwell type dampers at structural level. Those approaches typically do not impose explicit limits on pressure, cavitation or temperature [36, 9, 61, 8].
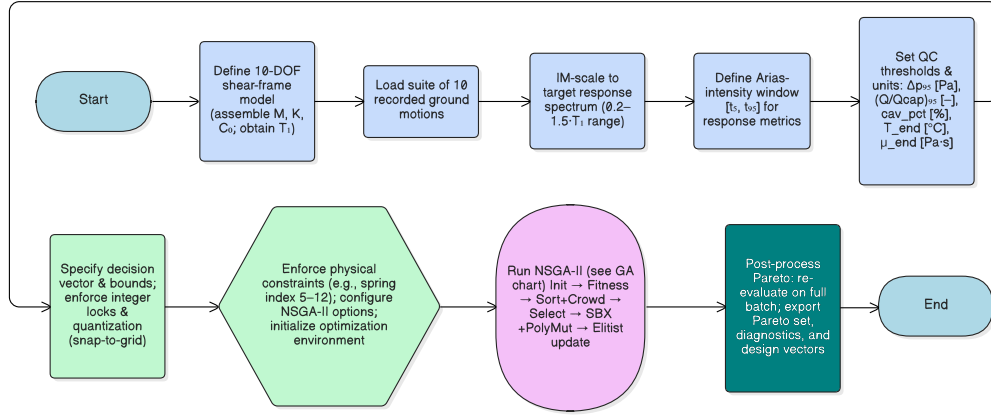

Figure 1: Overall methodological workflow: (Phase 1) input preparation and ground-motion processing, (Phase 2) GA setup and definition of decision variables, objectives and safety constraints, and (Phase 3) optimisation loop and Pareto-front extraction.

Finally, we examine the resulting Pareto fronts and summarise the main design trends. Near optimal solutions tend to cluster around medium piston diameters, multiple small orifices, intermediate oil viscosity and moderate heat transfer capacity. We discuss how these patterns can be distilled into design charts or surrogate models that complement current code oriented practice and placement studies [11, 33, 23]. The overall three phase workflow, from record processing and intensity measure selection through genetic algorithm setup with hydraulic and thermal safety constraints to multi objective optimisation and Pareto front analysis, is summarised in Figure 1 and detailed in the following sections.

2. Methods: Physical & Numerical Modelling

Figure 2 shows the n-DOF shear frame with a roof level FVD considered in this study. We used a detailed numerical model that coupled the n-DOF
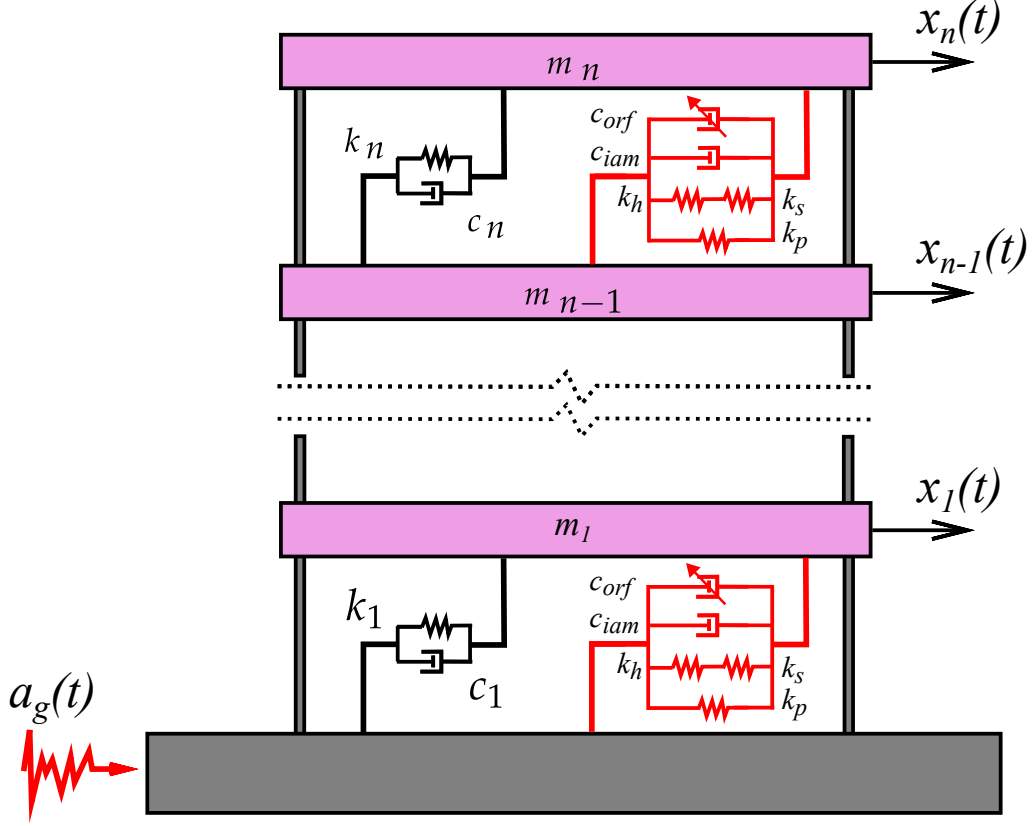
Figure 2: Schematic diagram of the n storey shear frame equipped with a roof level fluid viscous damper (FVD).

structural dynamics of the frame with the nonlinear thermal and hydraulic behaviour of the damper. In this model we did not rely on simplified phenomenological laws such as $F = C|\dot{u}|^{\alpha}$. Instead, the FVD submodel was mechanistic and included three main components. First, it described orifice hydraulics with a Reynolds-dependent discharge coefficient $C_d(\text{Re})$ and jet loss scaling $\Delta p \propto Q^2$ [57, 30, 44]. Second, it used a physics-based cavitation limiter implemented as a differentiable soft minimum between the jet candidate and an effective vapour threshold, consistent with orifice cavitation inception criteria [18]. Third, a two-node thermal block coupled temperature to viscosity and density, so that both $c_{\text{lam}}(T)$ and $C_d(\text{Re}(T))$ responded to heating [57, 61].

Classical $F = C|\dot{u}|^{\alpha}$ laws lump laminar and jet mechanisms and cannot

track pressure, cavitation and thermal safety under pulse type demands. For sharp edged short orifices in the relevant Re range, Δp follows a quadratic Q law with C_d varying with Re and geometry [57, 30, 44]. Keeping linear viscous losses in a parallel branch avoids double counting inside the orifice drop. Cavitation onset places a physical cap tied to vapour pressure and local accelerations [18], and practical FVD design and qualification likewise impose explicit pressure and capacity limits that we carried forward into the quality control metrics [61, 3, 49].

This coupling gave a stiff, coupled system of ordinary differential equations that advanced both the structural degrees of freedom and the damper temperatures at the same time. We integrated this system with the MATLAB solver `ode15s`. We used `RelTol = 1.0e-3` and `AbsTol = 1.0e-6`. In trial runs, these settings kept the damper response stable even in the stiffest parts of the motion. After each analysis, we evaluated all performance and safety metrics (PFA, IDR, pressure, temperature) over the significant duration interval from t_5 to t_{95} of the ground motion.

2.1. Structural model

We modelled a ten storey benchmark frame as a planar shear system with one lateral degree of freedom (DOF) per floor, because the lateral response is dominated by interstorey drift in the first mode. Let $\boldsymbol{x}(t) \in \mathbb{R}^{10}$ denote the relative floor displacements with respect to the moving base, and let $\boldsymbol{r} = \boldsymbol{1} \in \mathbb{R}^{10}$ be the base excitation influence vector. The equations of motion are

$$\boldsymbol{M}\,\ddot{\boldsymbol{x}}(t) + \boldsymbol{C}_0\,\dot{\boldsymbol{x}}(t) + \boldsymbol{K}\,\boldsymbol{x}(t) + \boldsymbol{f}_{\mathrm{d}}(t) = -\,\boldsymbol{M}\,\boldsymbol{r}\,a_g(t), \qquad (1)$$

where $\boldsymbol{M}$, $\boldsymbol{C}_0$ and $\boldsymbol{K}$ are the mass, structural damping and stiffness matrices, and $\boldsymbol{f}_{\mathrm{d}}(t)$ collects the nodal forces contributed by the devices. Table A.3 in Appendix A lists the storey masses, stiffnesses and damping ratios used to assemble these matrices, together with the modal notation adopted for intensity scaling.

We introduce the first difference (incidence) operator $\boldsymbol{B} \in \mathbb{R}^{9 \times 10}$ so that

$$\Delta \boldsymbol{x}(t) = \boldsymbol{B}\,\boldsymbol{x}(t), \qquad \Delta \dot{\boldsymbol{x}}(t) = \boldsymbol{B}\,\dot{\boldsymbol{x}}(t), \qquad (2)$$

and storey drift and drift rate follow directly from matrix multiplication. If $\boldsymbol{f}_{\mathrm{story}}(t) \in \mathbb{R}^9$ stacks the forces delivered by devices acting between floors, the associated nodal contribution assembles as

$$\boldsymbol{f}_{\mathrm{d}}(t) = \boldsymbol{B}^{\mathsf{T}}\,\boldsymbol{f}_{\mathrm{story}}(t). \qquad (3)$$

Absolute floor accelerations are defined as

$$\boldsymbol{a}_{\mathrm{abs}}(t) = \ddot{\boldsymbol{x}}(t) + \boldsymbol{r}\, a_g(t), \tag{4}$$

and the roof peak floor acceleration (PFA) is evaluated on the Arias window $[t_5, t_{95}]$ as

$$\mathrm{PFA} = \max_{t \in [t_5, t_{95}]} \left| \boldsymbol{e}_{10}^{\mathsf{T}} \boldsymbol{a}_{\mathrm{abs}}(t) \right|. \tag{5}$$

For a uniform storey height h, the maximum interstorey drift ratio (IDR) is

$$\mathrm{IDR} = \max_{t \in [t_5, t_{95}]} \left\| \frac{\Delta \boldsymbol{x}(t)}{h} \right\|_{\infty}. \tag{6}$$

Details of the tridiagonal assembly of $\boldsymbol{K}$ and $\boldsymbol{C}_0$ from the storey parameters, and of the modal notation used for intensity scaling (including the first-mode period T_1), are given in Appendix A, in particular Table A.3.

2.2. Damper physics

The storey device is described by two branches in parallel: a linear elastic branch that collects the overall axial compliance and a hydraulic branch that carries the orifice flow, as indicated in Figure 3.
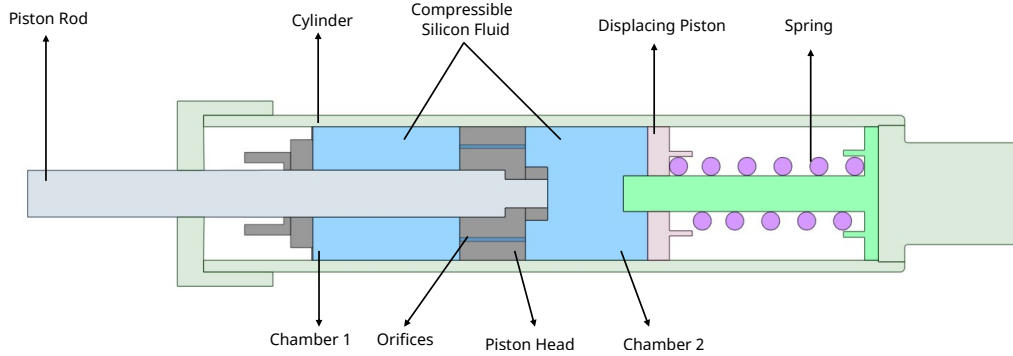

Figure 3: Schematic section of the fluid viscous damper (FVD). The piston head separates Chamber 1 and Chamber 2 and carries the orifices; the working fluid is a compressible silicone oil [56, 45], and a coil spring in parallel provides the stiffness k_{sd}.

With the storey drift $\Delta x(t)$ and drift rate $\Delta \dot{x}(t)$ defined as

$$\Delta x(t) = x_{i+1}(t) - x_i(t), \qquad \Delta \dot{x}(t) = \dot{x}_{i+1}(t) - \dot{x}_i(t), \tag{7}$$

8

and with A_p the piston area and A_o the total orifice area ($A_o = n_{\text{orf}} \pi d_o^2 / 4$), the storey force is written as

$$F_{\text{story}}(t) = F_{\text{elastic}}(t) + F_{\text{laminar}}(t) + F_{\text{orifice}}(t), \tag{8}$$

where the elastic and laminar contributions read

$$F_{\text{elastic}}(t) = k_{sd} \, \Delta x(t), \qquad F_{\text{laminar}}(t) = c_{\text{lam}}(T) \, \Delta \dot{x}(t). \tag{9}$$

In the elastic branch, k_{sd} gathers the compliance of the hydraulic assembly and the coil spring; Appendix A reports the geometric relations used to compute this stiffness.

A positive Δx increases the volume of the upper chamber and reduces the volume of the lower chamber, and the associated algebraic flow is counted as positive from the upper side to the lower side. For the ten storey frame considered in Section 2.1, one equivalent damper element with $n_{\parallel} = 1$ is assigned to each of the nine interstorey levels. Section 3 varies the damper parameters within this single equivalent layout, so the same parameter set is used for all nine devices. This $n_{\parallel} = 1$ element represents the total hydraulic circuit for that storey. In a practical installation where several physical cylinders act in parallel, their contributions (for example A_p, A_o, hA) are lumped into this equivalent element to avoid redundant design variables. For a regular plan building, the same damper design is adopted for the orthogonal (Y) direction.

Orifice hydraulics: jet loss with $C_d(\text{Re})$ (no linear drop inside Δp)

The safety metric $(Q/Q_{\text{cap}})_{95}$ requires a reference flow capacity for the orifice. We therefore define the theoretical orifice flow capacity under a nominal design pressure cap Δp_{cap} as

$$Q_{\text{cap}} = C_d^\infty A_o \sqrt{\frac{2 \, \Delta p_{\text{cap}}}{\rho(T)}}. \tag{10}$$

The design pressure cap is taken as $\Delta p_{\text{cap}} = \phi \, p_{\text{work}}$ with $\phi = 1.5$, where p_{work} is the manufacturer rated maximum working pressure [22]. When no project specific rating is available, we set $\Delta p_{\text{cap}} = 20\,\text{MPa}$, which falls in the lower half of the typical range reported for seismic FVD orifices (about 14-69 MPa). This choice gives roughly 1.5 times the working pressure, in line with hydraulic pressure test practice [22].

The saturated flow used in the jet loss term is

$$Q_{\text{sat}}(\Delta \dot{x}) = Q_{\text{cap}} \tanh\left(\frac{A_p}{Q_{\text{cap}}} \sqrt{\Delta \dot{x}^2 + v_\varepsilon^2}\right), \qquad v_\varepsilon > 0. \tag{11}$$

Only the quadratic (jet) head loss contributes to the orifice pressure candidate, in line with single phase orifice behavior,

$$\Delta p_{\text{kv}}(Q_{\text{sat}}, T) = \frac{\rho(T) \, Q_{\text{sat}} \, |Q_{\text{sat}}|}{2 \, [C_d(\text{Re}) \, A_o]^2}, \tag{12}$$

which reflects the measured $\Delta p \propto Q^2$ (equivalently $Q \propto \sqrt{\Delta p}$) relationships for sharp, short orifices at relevant Reynolds numbers [13, 1, 26]. Linear viscous losses act only through the parallel laminar branch $c_{\text{lam}}(T)$ in Eq. (9); embedding an additional linear drop inside Δp would double count the same mechanism.

The Reynolds number and the discharge coefficient are written as

$$\text{Re} = \frac{\rho(T) \, |Q_{\text{sat}}| \, d_o}{\mu(T) \, A_o}, \qquad C_d(\text{Re}) = C_d^\infty - \frac{C_d^\infty - C_d^0}{1 + \left(\text{Re}/\text{Re}_0\right)^{p_{\text{exp}}}}, \tag{13}$$

with C_d clamped to admissible bounds. Experiments show that the functional relation between C_d and Re and the onset of a high Reynolds plateau depend on geometry and operating conditions [41, 38, 5, 25]. In this study we hold the transition scale fixed at $\text{Re}_0 = 1000$ to avoid over parameterization and identifiability issues in the twelve dimensional design space; Appendix Table A.5 lists this value together with the supporting references.

For diagnostics and for the explicit viscous branch in Eq. (9), the laminar network is represented by its equivalent flow resistance R_{lam}. The resulting laminar coefficient c_{lam} follows from the standard hydraulic to mechanical equivalence $c_{\text{lam}} = R_{\text{lam}} A_p^2$:

$$R_{\text{lam}}(T) = \frac{128 \, \mu(T) \, L_{\text{ori}}}{\pi \, d_o^4} \frac{1}{n_{\text{orf}}}, \qquad c_{\text{lam}}(T) = R_{\text{lam}}(T) \, A_p^2, \tag{14}$$

so that $F_{\text{laminar}}(t) = c_{\text{lam}}(T) \, \Delta \dot{x}(t)$. The resistance R_{lam} does not enter Eq. (12); there is no linear drop inside Δp.

Cavitation limiter (physical model)

We model cavitation by imposing a smooth lower bound on the orifice pressure. An upstream pressure proxy is obtained from the elastic term relative to ambient:

$$p_\uparrow(t) = p_{\text{amb}} + \frac{|F_{\text{elastic}}(t)|}{A_p}. \tag{15}$$

Comparing $p_\uparrow$ to an effective vapour threshold defines the cavitation limited drop,

$$\Delta p_{\text{cav}}(t) = \max\{(p_\uparrow(t) - p_{\text{cav,eff}}) \cdot \text{cav\_sf}, 0\}, \tag{16}$$

and the effective orifice pressure is taken as the differentiable minimum

$$\Delta p_{\text{eff}} = \text{softmin}_\varepsilon(\Delta p_{\text{kv}}, \Delta p_{\text{cav}}). \tag{17}$$

The cavitation fraction over the Arias window is the time ratio for which $\Delta p_{\text{kv}} > \Delta p_{\text{cav}}$.

Room temperature silicone oils have very low vapour pressures, well below $1\,\text{kPa}$ at $25\,°\text{C}$, and cavitation inception is strongly influenced by dissolved gas and surface nuclei. Degassing protocols in silicone oil Venturi experiments markedly change inception, which underscores the role of gas content; diffusion driven nucleation from surface nuclei explains why inception can occur at absolute pressures that are still relevant for engineering applications [46, 27]. Manufacturer property sheets for PDMS damper oils report similarly low vapour pressures over the working temperature range [56, 45]. On that basis we place the effective threshold $p_{\text{cav,eff}}$ in the kilopascal range, applying a conservative safety factor above the pure vapour level so that the limiter flags only physically plausible inception in civil scale FVDs.

To keep the right hand side differentiable for stiff time integration and for gradient based penalties, we use the log sum exp smooth minimum

$$\text{softmin}_\varepsilon(a, b) = -\varepsilon \, \log(e^{-a/\varepsilon} + e^{-b/\varepsilon}),$$

which monotonically approaches $\min(a, b)$ as $\varepsilon \downarrow 0$ and removes non physical kinks while preserving the correct limiting behavior [16].

The hydraulic contribution to the storey force is

$$F_{\text{orifice}}(t) = \Delta p_{\text{eff}}(t) \, A_p \, \frac{\Delta \dot{x}(t)}{\sqrt{\Delta \dot{x}^2(t) + v_\varepsilon^2}}. \tag{18}$$

Linear (laminar) losses act only through $c_{\text{lam}}(T)$ in F_{laminar}; the orifice pressure uses the jet term with cavitation limiting, and no linear drop is embedded in Δp.

Thermal block (coupled viscosity feedback)

A compact two node energy balance (oil T_o, steel or cylinder T_s) is advanced concurrently with the structural state. This ensures that the temperature dependent viscosity $\mu(T)$ is updated inside the force evaluation and feeds back immediately into $c_{\text{lam}}(T)$ and the Reynolds dependent $C_d(\text{Re}(T))$:

$$C_o \dot{T}_o = P_{\text{loss}} - hA_{o\leftrightarrow s}(T_o - T_s) - hA_{o\leftrightarrow\text{env}}(T_o - T_\infty), \qquad (19)$$

$$C_s \dot{T}_s = \qquad + hA_{o\leftrightarrow s}(T_o - T_s) - hA_{s\leftrightarrow\text{env}}(T_s - T_\infty). \qquad (20)$$

To keep the number of thermal parameters manageable, all three exchange coefficients in Eqs. (19)–(20) are linked to the single optimization variable hA (total thermal conductance) listed in Table 2. We adopt a lumped model with

$$hA_{o\leftrightarrow s} = hA_{o\leftrightarrow\text{env}} = hA_{s\leftrightarrow\text{env}} = hA,$$

and no additional fixed baseline value is listed in the Appendix. Consistent with the three term force split, the instantaneous mechanical power is the sum of the laminar and orifice contributions (with no linear drop inside Δp):

$$P_{\text{loss}}(t) = \underbrace{c_{\text{lam}}(T_o)\,\Delta\dot{x}^{\,2}(t)}_{P_{\text{laminar}}} + \underbrace{\Delta p_{\text{eff}}(t)\,|Q_{\text{sat}}(t)|}_{P_{\text{orifice}}} \geq 0. \qquad (21)$$

The split in Eq. (21) follows standard hydraulic energetics. The laminar branch dissipates mechanical power as $P_{\text{laminar}} = c_{\text{lam}}(T_o)\,\Delta\dot{x}^{\,2}$, while the orifice branch converts hydraulic power $P = \Delta p_{\text{eff}}\,|Q_{\text{sat}}|$ into heat. Their sum gives the mechanical to thermal conversion that drives the two node balance in Eqs. (19)–(20). This is consistent with the mechanical energy balance for short, sharp edged orifices, $Q = C_d(\text{Re})\,A_o\sqrt{2\,\Delta p/\rho}$, hence $\Delta p \propto Q^2$; here C_d depends on Re at low to intermediate values and approaches a plateau as Re increases [57, 12, 5].

Temperature dependent properties follow smooth laws:

$$\mu(T) = \mu_{\text{ref}}\,\exp\big(b_\mu(T - T_{\text{ref}})\big), \qquad \rho(T) = \frac{\rho_{\text{ref}}}{1 + \alpha_\rho(T - T_{\text{ref}})}. \qquad (22)$$

For PDMS silicone oils, the viscosity temperature relation is well captured over engineering ranges (roughly 20 to $100\,°\text{C}$ and low to moderate shear) by log linear or Arrhenius type fits, which motivates the exponential form in Eq. (22). We calibrate the fit around $T_{\text{ref}} = 25\,°\text{C}$ using manufacturer data for the specific oil grade in the zero shear region. The same dataset provides

the density slope α_ρ used in Eq. (22), so that $\rho(T)$ and therefore $\mathrm{Re}(T)$ and $C_d(\mathrm{Re}(T))$ respond consistently to heating [50, 55, 59, 56, 45]. The property slopes b_μ, α_ρ and the optional b_ρ in Eq. (22) were obtained by least squares fits to the same manufacturer data.

The accumulated dissipation reported on the Arias window is

$$
\begin{aligned}
E_{\mathrm{mech}} &= \int_{t_5}^{t_{95}} P_{\mathrm{loss}}(t)\,\mathrm{d}t \\
&= \int_{t_5}^{t_{95}} \left(c_{\mathrm{lam}}(T_o)\,\Delta\dot{x}^2(t) + \Delta p_{\mathrm{eff}}(t)\,\big|Q_{\mathrm{sat}}(t)\big| \right) \mathrm{d}t.
\end{aligned}
\tag{23}
$$

The present hydro thermal FVD model is not recalibrated against a new, dedicated self-heating test campaign for this specific hardware. Instead, its building blocks and parameter ranges are anchored in specimen-scale self-heating experiments and CFD-based damper models from the literature. Laka and Zahrai [37] and Zhang et al. [60] report full-scale tests on commercial and gap-type viscous dampers in which coupled hydrothermal models reproduce measured force, temperature and energy histories with good agreement. High-fidelity CFD simulations with heat transfer, such as those by Frings et al. [24] and Zhong et al. [61], resolve the same laminar/jet split, Reynolds-dependent discharge behaviour and viscosity–temperature laws that underlie Eqs. (10)–(23). In the present work we follow these studies at the level of constitutive assumptions and property fits (for example, $\mu(T)$ and $\rho(T)$ are calibrated to manufacturer data over the same temperature range), but recast the device into an ODE-only, computationally light form that can be embedded directly in a multi-record, multi-objective optimisation at building scale. In that sense, model validation is indirect and literature-based: we rely on the experimental and CFD evidence cited above to support the physical fidelity of the hydro thermal mechanisms, and then examine how a damper that obeys the same mechanisms behaves when tuned within a realistic design envelope and coupled to a ten-storey frame under strong ground motions.

Appendix A consolidates the fixed coefficients, bounds and geometric data used in the damper model. Tables A.5 and A.6 list, respectively, the physical constants (including the $C_d(\mathrm{Re})$ transition scale, cavitation-related parameters and temperature-dependent property slopes) and the derived stiffnesses and resistances that enter k_{sd} and $c_{\mathrm{lam}}(T)$. All quantities use SI units, with Q in $\mathrm{m^3\,s^{-1}}$, Δp in Pa and areas in $\mathrm{m^2}$.

2.3. Time integration

We integrated the coupled frame and damper model with a stiff variable step ODE scheme. The state vector collects the structural displacements and velocities together with the two thermal degrees of freedom, while the hydraulic quantities are evaluated algebraically inside the right hand side. With $\boldsymbol{x}(t) \in \mathbb{R}^{10}$ the relative floor displacements and $\boldsymbol{v}(t) = \dot{\boldsymbol{x}}(t)$, the first order form reads

$$\boldsymbol{z}(t) = \begin{bmatrix} \boldsymbol{x}^{\mathsf{T}}(t) & \boldsymbol{v}^{\mathsf{T}}(t) & T_o(t) & T_s(t) \end{bmatrix}^{\mathsf{T}},$$

$$\dot{\boldsymbol{x}}(t) = \boldsymbol{v}(t),$$

$$\dot{\boldsymbol{v}}(t) = -\boldsymbol{M}^{-1}\big(\boldsymbol{C}_0\boldsymbol{v}(t) + \boldsymbol{K}\boldsymbol{x}(t) + \boldsymbol{f}_{\mathrm{d}}(t)\big) - \boldsymbol{r}\,a_g(t), \tag{24}$$

where $\boldsymbol{f}_{\mathrm{d}}(t) = \boldsymbol{B}^{\mathsf{T}}\boldsymbol{f}_{\mathrm{story}}(t)$ and $\boldsymbol{f}_{\mathrm{story}}(t)$ is returned by the mechanistic device model from the instantaneous storey drift and drift rate.

At each evaluation time, the damper routine forms $\Delta\dot{x}(t) = \boldsymbol{B}\,\boldsymbol{v}(t)$ and uses the current oil temperature to compute the saturated flow Q_{sat} (Eq. (11)), the Reynolds number and discharge coefficient $C_d(\mathrm{Re})$ (Eq. (13)), the jet candidate Δp_{kv} (Eq. (12)) and the cavitation limited pressure Δp_{eff} (Eq. (17)). The storey force is then assembled as the sum of the elastic term, the laminar branch and the orifice contribution with smoothed sign (Eqs. (9) and (18)).

The base acceleration $a_g(t)$ is obtained by linear interpolation of the sampled record. Large pressure gradients and the cavitation limiter make the device equations stiff at high velocities, so we used the MATLAB solver `ode15s` for all runs. In all runs we set RelTol $= 1.0 \times 10^{-3}$ and AbsTol $= 1.0 \times 10^{-6}$; in practice this combination stabilised the damper response without causing many rejected steps. The solution is evaluated on the native record grid, but response measures are extracted only on the Arias window $[t_5, t_{95}]$ to exclude the start up drift and late coda.

The two node thermal block in Eqs. (19)–(20) is advanced together with the structural state and feeds back through $\mu(T_o)$ and $\rho(T_o)$. The mechanical power that drives the thermal balance is $P_{\mathrm{loss}}(t)$ in Eq. (21), and the accumulated dissipation on $[t_5, t_{95}]$ is E_{mech} in Eq. (23).

At t_0 the frame is taken at rest, so $\boldsymbol{x}(t_0) = \boldsymbol{0}$ and $\boldsymbol{v}(t_0) = \boldsymbol{0}$. Device multiplicity and storey activity masks are applied algebraically: areas and linear coefficients scale with $n_{\parallel}$, and inactive storeys are set to zero. This keeps the assembled system sparse and avoids modifying the core integrator. Additional numerical safeguards, such as the soft minimum sharpness and the small velocity regularisation in Eq. (18), are listed in Appendix A.

2.4. Ground motion processing and scaling

We used a set of ten recorded horizontal ground motions for all nonlinear analyses. Each accelerogram was converted to SI units (m/s^2) and de trended, and a mild high pass filter (for example $f_c = 0.05$ Hz) was applied when baseline drift was visible.

Table 1: Selected earthquake records used in this study (horizontal components).

Code	Earthquake name	Year	Station / Component	M_w	Distance (km)	PGA (g)
KB95	Kobe	1995	KJMA / KJMA-000	6.9	0.96	0.833
NR94	Northridge	1994	Sylmar County Hospital / 360	6.7	9.90	0.842
IR80	Irpinia (Italy)	1980	Sturno (STN) / STU270	6.9	6.78	0.320
MJ90	Manjil	1990	Abbar / ABBAR-L	7.3	12.55	0.510
LP89	Loma Prieta	1989	Calaveras Reservoir / CLR180	6.9	35.28	0.110
CC99	Chi–Chi	1999	TCU078 / 90°	7.6	8.30	0.442
MR23	Kahramanmaras (Türkiye)	2023	TK 4614 / HNE	7.8	9.80	2.209
TB78	Tabas	1978	Tabas / H2	7.4	2.10	0.862
CM92	Cape Mendocino	1992	Petrolia / H2	7.0	8.20	0.662
CH07	Chuetsu	2007	Joetsu Kakizaki / 65010EW	6.8	9.43	0.580

Sources: PEER NGA-West2 (all but MR23) and AFAD Strong Motion Databases (MR23). Distances use closest-to-fault values (R_{rup}) when available and all PGA entries are reported in g; Chi–Chi and Kahramanmaras were converted from cm/s^2 using $1\,g = 980.665$ cm/s^2. Codes coincide with the internal labels used in the optimisation runs (MR23 corresponds to AFAD TK 4614, HNE component), and the mix intentionally retains high-PGA near-fault motions (for example MR23 at $2.209\,g$) to exercise the pressure, temperature and cavitation limits enforced by the QC metrics.

To place all records at a common intensity level, each motion was scaled to a target intensity $\mathrm{IM}_\star$. The chosen measure is the band averaged geometric mean of the 5% damped pseudo spectral acceleration, evaluated on N linearly spaced periods within a band centred on the first mode period T_1, from T_1/γ to γT_1:

$$\mathrm{IM}_{\mathrm{band}} = \exp\left(\frac{1}{N} \sum_{k=1}^{N} \ln S_a^{(5\%)}(T_k) \right), \qquad T_k \in [T_1/\gamma, \ \gamma T_1]. \qquad (25)$$

This band averaged quantity belongs to the family of S_a based measures that work with logarithmic ordinates over a period band. By centring the band on T_1, it remains efficient and reasonably sufficient for first mode dominated shear frames. It is also directly comparable to Sa,avg or AvSv type measures used in record selection and scaling [54]. The Arias window $[t_5, t_{95}]$ is used consistently when computing peak or percentile response measures, in line with significant duration definitions based on D_{5-95} [17, 32].

For each record, the scale factor

$$s = \frac{\text{IM}_\star}{\text{IM}_{\text{band}}},$$

clamped to the admissible range $[0.2, 2.2]$, is applied to obtain the scaled motion $\tilde{a}_g(t) = s\, a_g(t)$. The same scaled input is used for the bare frame and for all damper configurations, so that differences in response stem from the device design rather than from changes in the excitation.

As summarised in Table 1, the record set deliberately mixes near-fault high-PGA events (for example MR23 at $2.209\,\text{g}$) with more moderate motions. This combination ensures that the pressure, temperature, capacity and cavitation limits enforced by the QC metrics are exercised over a broad range of demands.

All performance measures (for example PFA, IDR and the damper level safety metrics) are evaluated on the 5%-95% Arias intensity window $[t_5, t_{95}]$. For each design, per record quantities are then averaged over the ten motions to form the optimisation objectives.

3. Optimization Framework

We solved a safety first, lexicographic multi objective optimisation problem. Candidate designs were ordered by the triplet $(f_{\text{pen}}, f_1, f_2)$, with $f_1 = \langle \text{PFA} \rangle$ and $f_2 = \langle \text{IDR} \rangle$, and we examined the Pareto trade-off in the (f_1, f_2) plane for solutions with $f_{\text{pen}} \approx 0$. Figure 4 sketches the workflow. The aim was to identify device parameter vectors $\boldsymbol{d}$ that reduce both the record mean roof peak floor acceleration (PFA) and the record-mean maximum interstorey drift ratio (IDR). All metrics were evaluated on responses restricted to the Arias-intensity window $[t_5, t_{95}]$ for a fixed set of ten intensity-scaled ground motions.
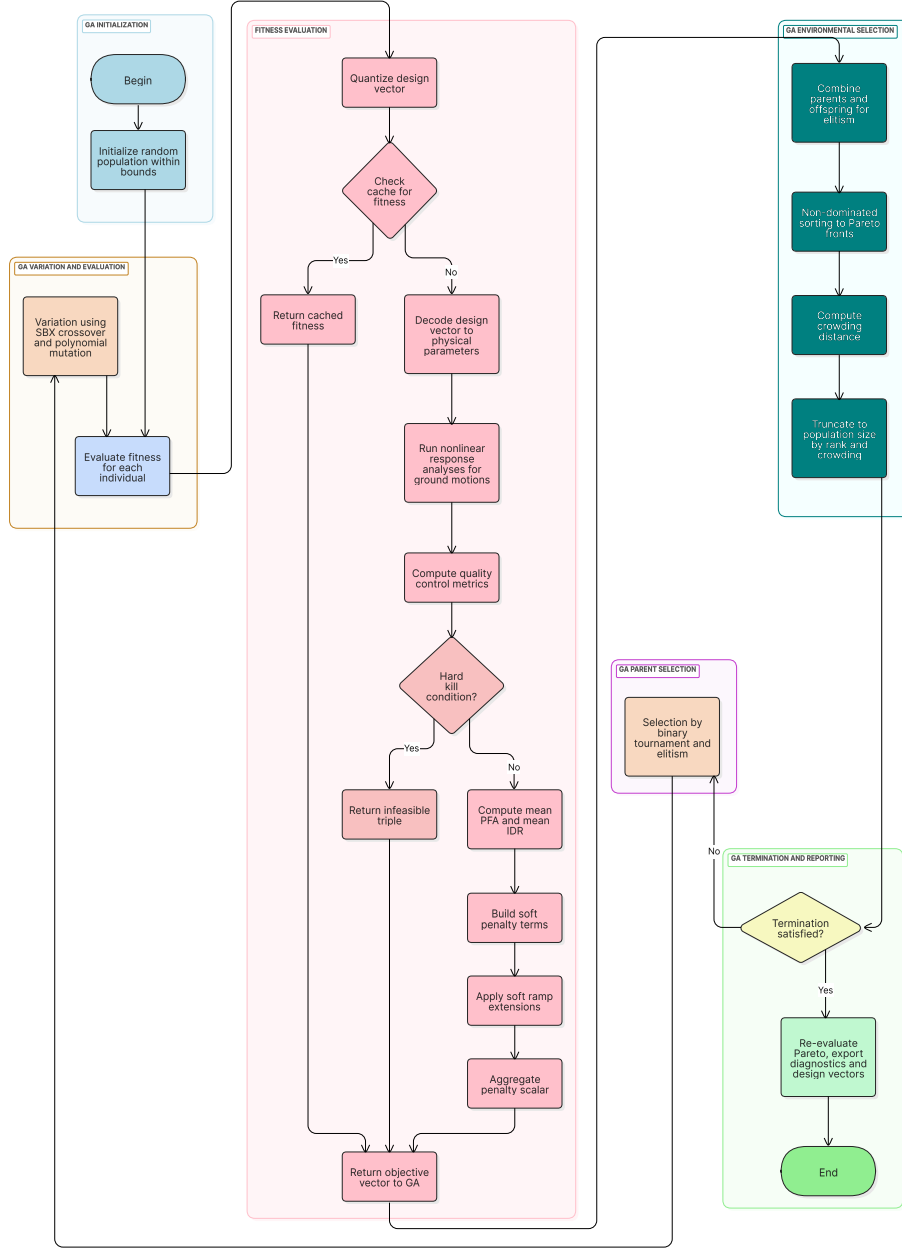
16

Figure 4: Flowchart of the NSGA-II optimization process, illustrating population evaluation, safety screening (hard constraints), and multi objective ranking $(f_{\mathrm{pen}}, f_1, f_2)$.

3.1. Objectives and Safety Constraints

The primary performance objectives are the record wise arithmetic means of the structural demands:

$$\min_{\boldsymbol{d}\in\mathcal{X}} \quad f_1(\boldsymbol{d}) = \frac{1}{10}\sum_{j=1}^{10}\mathrm{PFA}_j(\boldsymbol{d}), \qquad f_2(\boldsymbol{d}) = \frac{1}{10}\sum_{j=1}^{10}\mathrm{IDR}_j(\boldsymbol{d}), \qquad (26)$$

where $\mathcal{X}$ is the admissible (manufacturable and physically valid) design space.

Hydraulic and thermal safety is enforced using a two tier policy. First, a hard screen discards any design that violates the fixed thresholds (see boxed text) on any record. Second, feasible designs are ranked lexicographically using the vector

$$\left[\, f_{\mathrm{pen}}, \ f_1, \ f_2 \,\right].$$

This ordering puts safety in front of the structural objectives. The penalty function f_{pen} is a smooth aggregate of normalised safety excesses; it is zero when all checks are satisfied and increases monotonically with any near violation, while remaining differentiable for the solver.

Fixed QC thresholds (per record, on Arias window; see also Appendix Table A.4).

- Max. 95th percentile pressure: $\Delta p_{95} \leq 4.0 \times 10^7\,\mathrm{Pa}$

- Max. 95th percentile flow ratio: $(Q/Q_{\mathrm{cap}})_{95} \leq 0.90$

- Max. cavitation time fraction: $\mathrm{cav}_{\mathrm{pct}} \leq 0.5\%$

- Max. end of window temperature: $T_{\mathrm{end}} \leq 75\,^{\circ}\mathrm{C}$

- Min. end of window viscosity: $\mu_{\mathrm{end}} \geq 0.70\,\mathrm{Pa\,s}$

The thresholds in the QC box were set conservatively to match the operating envelope of industrial FVDs and to balance device longevity, model validity and material constraints. They are deliberately strict and consistent with the safety first ordering of objectives.

We motivate the main limits as follows. (i) The internal pressure bound ($\Delta p_{95} \leq 4.0 \times 10^7\,\mathrm{Pa}$, about $40\,\mathrm{MPa}$) was chosen to preserve the mechanical integrity of the cylinder and seals. For comparison, high performance damper seals are rated up to roughly $275\,\mathrm{MPa}$, and burst tests for civil devices often target pressures on the order of $140\,\mathrm{MPa}$ [53]. (ii) The thermal limits

($T_{\text{end}} \leq 75\,^{\circ}\text{C}$ and $\mu_{\text{end}} \geq 0.70\,\text{Pa\,s}$) serve a dual purpose. They keep the device within the functional range reported for silicone fluid dampers (typically from about -40 to $+70\,^{\circ}\text{C}$) [39] and avoid excessive thermal thinning or degradation, which becomes more likely above roughly $90\,^{\circ}\text{C}$. In this way the calibrated $\mu(T)$ and $C_d(\text{Re}(T))$ relations remain valid. (iii) The flow ratio cap $((Q/Q_{\text{cap}})_{95} \leq 0.90)$ leaves a ten percent headroom below the nominal orifice capacity. This margin keeps the device away from a choked regime in which compressibility or cavitation dominate and the response becomes highly nonlinear [14]. (iv) The cavitation policy $(\text{cav}_{\text{pct}} \leq 0.5\%)$ replaces an unrealistically strict zero tolerance requirement by a small, practical allowance that is insensitive to minor numerical noise. Cavitation is counted only when the pressure stays below the effective threshold $p_{\text{cav,eff}}$ by at least $0.5\,\text{kPa}$ for a holding time of $5\,\text{ms}$ or longer. This de minimis allowance means that brief numerical spikes are ignored, whereas any design that triggers sustained inception and cumulative damage or performance degradation [48] is still removed by the hard screen.

Designs breaching any bound are rejected by the hard screen; others are penalised softly via f_{pen}.

To ensure fairness, every candidate design $\boldsymbol{d}$ is evaluated against the same set of ten pre scaled ground motions and identical modelling and integration policies. No per record retuning is allowed, so the objective values reflect only changes in the device parameters. While the optimisation uses means, response dispersion is reported in Section 4 to support robust engineering choices.

3.2. Decision Variables and Bounds

The design vector $\boldsymbol{d}$ collects the twelve key parameters that control the hydraulic, elastic and thermal behaviour of the device:

$$\boldsymbol{d} = \big[d_o,\ n_{\text{orf}},\ C_d^0,\ C_d^\infty,\ p_{\text{exp}},\ L_{\text{ori}},\ hA,$$
$$D_p,\ d_w,\ D_m,\ n_{\text{turn}},\ \mu_{\text{ref}}\big]^{\mathsf{T}}. \tag{27}$$

where d_o is the orifice diameter, n_{orf} the number of parallel orifices (integer), $(C_d^0, C_d^\infty, p_{\text{exp}})$ the discharge law parameters, L_{ori} the orifice length, hA the total heat transfer conductance, $(D_p, d_w, D_m, n_{\text{turn}})$ the piston and spring geometry (with n_{turn} integer), and μ_{ref} the reference viscosity.

The feasible region $\mathcal{X}$ is a box constrained domain (Table 2) with integrality enforced on n_{orf} and n_{turn}. Bounds in Table 2 reflect manufacturability and

basic physics. The lower orifice diameter bound avoids sub millimetre drilling that would otherwise require EDM or laser processes and compromised tolerances, while the selected L_{ori}/d_o range keeps the device in a short, sharp edged orifice tube regime where $C_d(\mathrm{Re})$ exhibits a clear plateau and a predictable sensitivity to thickness and length to diameter ratio [2, 31, 47]. Spring geometry enforces a practical spring index $C = D_m/d_w$ in the conventional design range, supported by recent numerical and failure analyses of low index helical springs, to avoid buckling, excessive stress concentrations and premature fatigue [28, 51, 40, 58]. Integer constraints on n_{orf} and n_{turn} encode the physical multiplicity of orifices and active coils, while piston diameter bounds follow standard seal availability and machining constraints in industrial hydraulic cylinders.

Table 2: Optimization decision variables and bounds.

Symbol	Description	Lower	Upper	Units
d_o	Orifice diameter (per orifice)	0.000 80	0.003 50	m
n_{orf}	Parallel orifices *(integer)*	3	12	–
C_d^0	Discharge coefficient: laminar limit	0.55	0.95	–
C_d^∞	Discharge coefficient: turbulent limit	0.70	1.00	–
p_{exp}	$C_d(\mathrm{Re})$ transition exponent	0.90	1.60	–
L_{ori}	Orifice length	0.10	0.24	m
hA	Total thermal conductance	150	400	$\mathrm{W\,K^{-1}}$
D_p	Piston diameter	0.110	0.260	m
d_w	Spring wire diameter	0.008	0.020	m
$D_m^\dagger$	Spring mean diameter	0.080	0.200	m
n_{turn}	Active spring turns *(integer)*	6	15	–
μ_{ref}	Reference viscosity at T_{ref}	0.60	2.00	$\mathrm{Pa\,s}$

Manufacturability note. Bounds enforce drillable orifice diameters, short sharp edged orifice tube aspect ratios, practical spring index and seal compatible piston sizes. †Spring index defined as $C = D_m/d_w$.

The bi objective optimisation problem was solved with a Pareto based evolutionary solver of the NSGA II class. The algorithm used a population of 600 individuals and ran for 180 generations, and each candidate was evaluated over the full ground motion set. We adopted a crossover fraction of 0.90 with simulated binary crossover and Gaussian mutation (`MutationFcn=mutationgaussian`). The random seed was fixed

(rng(42,'twister')) so that the reported Pareto fronts and safety statistics can be reproduced.

After convergence, every non dominated design was re evaluated to collect extended safety and energy indicators (for example, pressure percentiles and energy partitions). These diagnostics were archived and form the basis of the analysis in Section 4.

4. Results and Discussion

This section reports the outcome of the multi-objective optimization and compares the Bare Frame (no dampers) with the Optimized System, defined as the knee-selected FVD from the Pareto front. We focus on how the optimised device reshapes the seismic demand profile, how it redistributes input energy between structure and damper, and whether it stays within the imposed safety margins.

4.1. Evaluation of Seismic Performance Enhancement

Figures 5–7 compare the Arias-window responses for the Bare Frame and the Optimized System. Figures 5 and 6 show, for a representative scaled input (MR23 in Table 1), the roof absolute acceleration and displacement histories over $[t_5, t_{95}]$. Figure 7 then summarises the storey-wise statistics. Across all ten records, the optimized configuration suppresses roof absolute acceleration and inter-storey drift, so that a larger share of the input energy is absorbed and dissipated within the dampers instead of being stored and repeatedly released in the frame.

The visual trends are condensed in Table 3. Record-averaged performance is taken from the post-optimization audit (Section 3): the Baseline row corresponds to the bare frame, and the Optimized row to the knee-selected design obtained from the Pareto set. Percentage gains are reported as

$$\Delta(\%) \;=\; 100 \, \frac{B - O}{B},$$

where B and O denote the baseline and optimized values of each response metric.

On this record set, the mean roof acceleration falls from $13.27 \, \mathrm{m/s^2}$ to $5.05 \, \mathrm{m/s^2}$, i.e. by about 60%. The mean maximum inter-storey drift ratio drops from 0.88% to 0.30% (about 65%). These reductions are broadly uniform along the height of the building rather than being concentrated at a

21

single storey, which is consistent with the first-mode-dominated response of the ten-storey frame.

Table 3: Record-averaged performance: Bare Frame vs. knee-selected Optimized FVD (from audit).

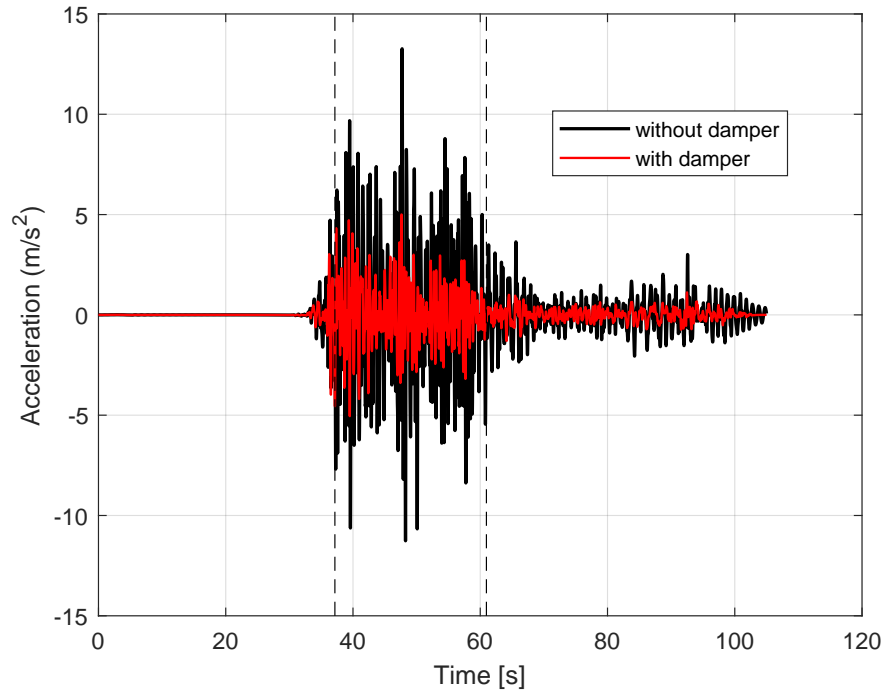| Design	$\overline{\text{PFA}}$ [m/s^2]	$\overline{\text{IDR}}$ [%]	ΔPFA [%]	ΔIDR [%]
Baseline (Bare Frame)	13.27	0.880	–	–
Optimized (Knee–FVD)	5.05	0.300	61.9	65.9

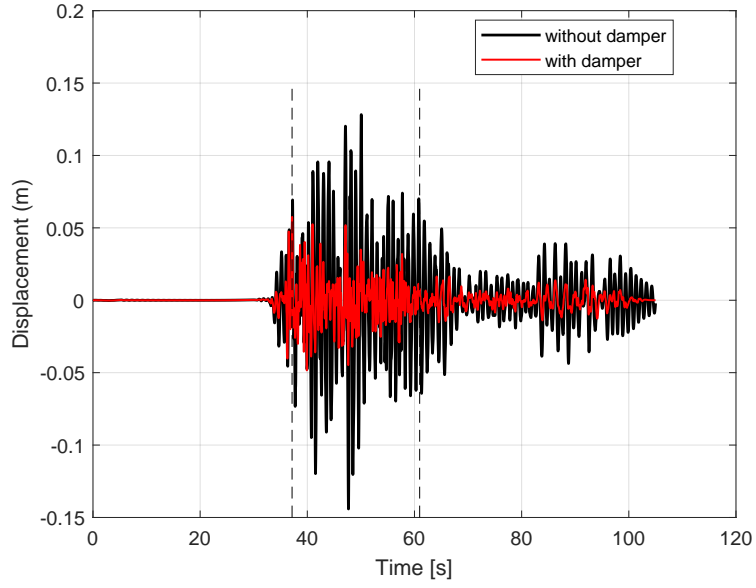Figure 5: Top–floor absolute acceleration ...

22
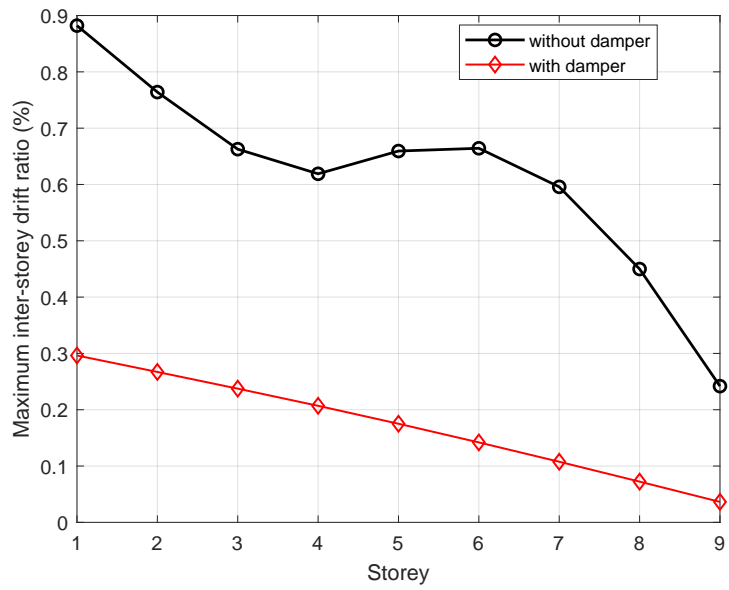
Figure 6: Top–floor displacement.

Figure 7: Storey–wise maximum inter–storey drift ratio.

23

4.2. Multi-Objective Trade-off Analysis and Safety Verification

Figure 8 displays the final non-dominated set in the objective space $\left(f_1=\langle\mathrm{PFA}\rangle,\ f_2=\langle\mathrm{IDR}\rangle,\ f_{\mathrm{pen}}\right)$. Many designs lie close to $f_{\mathrm{pen}}\approx 0$, indicating that a sizeable fraction of the Pareto front already satisfies the safety policy of Section 3.1. Within this feasible cluster, the marked knee solution offers a compromise between reducing structural demands and maintaining device-level margins.

Knee selection is carried out on the safe part of the front by first retaining only non-dominated designs with $f_{\mathrm{pen}}\approx 0$ and then working in the min, max normalised (f_1, f_2) plane spanned by this subset. In that reduced space, the chosen configuration is the point with the smallest Euclidean distance to the utopian corner $(0,0)$ under equal weights on the two objectives, so the selected design sits near the elbow of the Pareto cloud without favouring either PFA or IDR a priori.

While Table 3 summarises the objective values, Table 4 lists detailed safety indicators, energy partitions, and peak responses for the selected configuration, including roof displacement and acceleration. Table 5 reports the corresponding FVD parameters; in the discussion below, only a subset of these values is used to interpret the safety margins and the energy split.

Table 4: Knee-selected design: detailed safety, energy, and peak response indicators (from re-evaluation audit).

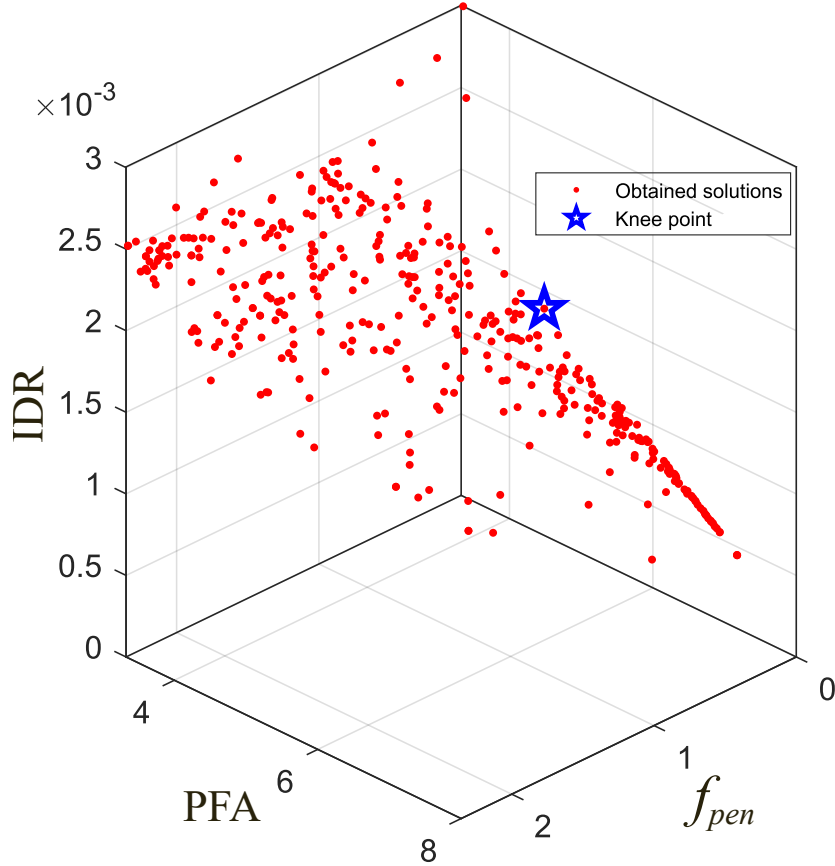| Design	$\mathrm{Disp}_{\mathrm{roof,peak}}$ [m]	$\mathrm{Acc}_{\mathrm{roof,peak}}$ [m/s^2]	dP95 [Pa]	$(Q/Q_{\mathrm{cap}})_{95}$	cav_%	T_{end} [°C]	μ_{end} [Pa s]	E_{orifice} [J]	E_{struct} [J]	P_{mech} [W]	E_{ratio}
Knee–FVD (Xbest)	0.0517	7.6273	5.98×10^6	0.634	0.00	74.1	0.70	3.52×10^7	2.15×10^7	1.48×10^6	1.63

Figure 8: NSGA–II Pareto front in $(f_1, f_2, f_{\text{pen}})$; the star marks the knee–selected design.

When the configuration in Table 5 is re-evaluated on the full ground-motion set, it satisfies all constraints listed in Section 3.1. As reported in Table 4, the 95th percentile pressure is about 6×10^6 Pa, which leaves a substantial margin below the 4.0×10^7 Pa cap chosen to protect seals and barrel under repeated loading. The flow-ratio indicator $(Q/Q_{\text{cap}})_{95} \approx 0.63$ remains under the $(Q/Q_{\text{cap}})_{95} \leq 0.90$ bound, so the orifice does not operate near its capacity limit for any record in the set. Under the adopted cavitation definition, the time fraction with $p < p_{\text{cav,eff}}$ is essentially zero, indicating that the device does not enter sustained cavitating regimes over the significant duration. The end-of-window temperature T_{end} stays below 75 °C, and the final viscosity $\mu_{\text{end}} = 0.70$ Pa s coincides with the imposed lower limit, keeping

Table 5: Optimized design parameters for the knee-selected FVD (corresponds to Table 4).

Symbol	Parameter	Value	Unit
d_o	Orifice diameter	0.00140	m
n_{orf}	Parallel orifices *(int)*	11	–
C_d^0	Discharge coeff. (laminar)	0.89	–
C_d^∞	Discharge coeff. (turbulent)	0.77	–
p_{exp}	$C_d(\text{Re})$ transition exp.	1.46	–
L_{ori}	Orifice length	0.185	m
hA	Total thermal conductance	228	W K^{-1}
D_p	Piston diameter	0.157	m
d_w	Spring wire diameter	0.014	m
D_m	Spring mean diameter	0.125	m
n_{turn}	Active spring turns *(int)*	10	–
μ_{ref}	Reference viscosity	1.46	Pa s

the operation within the calibrated range of the $\mu(T)$ and $C_d(\text{Re}(T))$ laws rather than relying on an excessively thinned fluid.

The audit also clarifies how the damper reshapes the energy path. Over the Arias window, the orifice branch dissipates on the order of 3.5×10^7 J, whereas the structural contribution is about 2.2×10^7 J. The resulting energy ratio $E_{\text{ratio}} \approx 1.6$ therefore favours the device: more seismic input is converted into heat inside the FVD than is cycled as recoverable strain energy in the frame. This shift in the energy split is consistent with the large reductions in $\langle\text{PFA}\rangle$ and $\langle\text{IDR}\rangle$ reported in Table 3.

The safety-first lexicographic search yields a dense set of feasible designs with $f_{\text{pen}} \approx 0$. Within this set, the selected FVD configuration achieves substantial record-averaged reductions in $\langle\text{PFA}\rangle$ and $\langle\text{IDR}\rangle$ (Table 3) while remaining within all pressure, flow-capacity, cavitation and thermal limits of the coupled model (Table 4). Taken together, the demand, safety and energy indicators suggest that the device operates away from marginal regimes, so the knee design provides a realistic starting point for further engineering refinement and eventual hardware implementation.

5. Conclusions

This paper has introduced a high-fidelity modelling and multi-objective design framework for fluid viscous dampers (FVDs) installed on a ten storey shear

frame. The model couples a mechanistic FVD description—with a Reynolds dependent discharge coefficient, a cavitation soft limiter and a two node thermal block with temperature dependent viscosity and density—directly to the structural equations of motion of the benchmark frame; in this way it goes beyond the classical $F = C|v|^\alpha$ laws and tracks pressure, flow and temperature histories explicitly [57, 30, 18, 61]. Seismic demand is represented by ten recorded horizontal ground motions scaled to a common band averaged geometric mean PSA centred on the fundamental period T_1, and all response and safety metrics are evaluated on the Arias intensity window $[t_5, t_{95}]$; the record set is deliberately enriched with near fault, high PGA events to probe robustness [54, 17, 32]. On top of this physical model, an NSGA-II search with safety first lexicographic ranking, $[f_{\text{pen}}, \langle \text{PFA} \rangle, \langle \text{IDR} \rangle]$, and fixed hydraulic and thermal QC thresholds links device parameters to safe, performance optimised FVD designs for this particular ten storey archetype.

For the knee selected configuration, the record mean roof PFA drops from 13.27 to 5.05 m/s^2 (about 60%), and the record mean maximum inter storey drift ratio from 0.88% to 0.30% (about 65%) over the ten intensity scaled motions (Table 3). Roof displacements and accelerations remain in a moderate range even for the most demanding near fault input, represented here by the Kahramanmaraş MR23 record with a PGA of 2.209 g; this record still gives controlled response, which is encouraging for a velocity dependent device (Table 1) [49, 3].

An energy audit shows that, on this benchmark, the orifice branch dissipates about 3.5×10^7 J per analysis, compared with roughly 2.2×10^7 J in the structural viscous branch (Table 4). This split corresponds to an energy ratio $E_{\text{ratio}} \approx 1.6$, so most of the seismic input is converted to heat in the damper instead of being cycled through the frame. In the knee selected design, the orifice jet loss term carries most of the dissipation, while the laminar branch regulates low velocity behaviour and adds a smaller, but non negligible, share to the thermal load; this picture is consistent with the power split

$$P_{\text{loss}} = c_{\text{lam}}(T_o) \, \Delta \dot{x}^2 + \Delta p_{\text{eff}} \, |Q_{\text{sat}}|$$

in Eq. (21) and with the audit in Table 4. The coupled thermal block raises the oil temperature to $T_{\text{end}} \approx 74$ °C with a terminal viscosity $\mu_{\text{end}} \approx 0.70$ Pa s; this shift increases the Reynolds number and moves $C_d(\text{Re})$ towards its high Re plateau, but stays within the imposed viscosity bound and within published property trends for PDMS silicone oils. At the same time, the

pressure and capacity indicators remain within their prescribed limits, with $dP95 \approx 6 \times 10^6$ Pa against a 40 MPa cap and $(Q/Q_{\mathrm{cap}})_{95} \approx 0.63 < 0.90$, and the cavitation time fraction stays below 0.5% of the Arias window under the adopted definition (Tables A.4 and 4) [13, 1, 26, 46]. Taken together, these results suggest that, when sized within a physically consistent thermal and hydraulic window, civil scale FVDs of the type modelled here can operate safely and efficiently under strong impulsive demands for the considered ten storey benchmark and record set, in line with recent experimental observations on seismic dampers.

The present framework is demonstrated on a single, planar, first mode dominated ten storey shear frame with one equivalent device per interstorey level and a single family of silicone oils. The damper model is assembled from literature based hydro thermal building blocks and calibrated against manufacturer property data rather than against a dedicated prototype test for this particular hardware, and the optimisation is run on a fixed set of ten horizontal ground motions. As such, the results should be read as a proof of concept for this archetype, not as a general recipe covering all FVD equipped buildings and bridges.

From an engineering standpoint, the optimized device sits in the middle of the explored design space and combines a moderate piston diameter, a relatively large number of small orifices, an intermediate reference viscosity and an intermediate thermal conductance; this mix yields substantial response reduction while keeping pressure and temperature in a conservative range (Table 5). Within the limits just discussed, the workflow can act as a physics-based complement to code-oriented procedures. For a chosen building archetype, an engineer may fix a target IM band level, set application-specific QC thresholds (for example, consistent with EN 15129 limits), and then use a multi-objective search to map out a family of safe and efficient FVD designs that can later be condensed into design charts or surrogate models for routine use [48, 53]. Future work should address the remaining gaps by (i) validating the coupled thermal and hydraulic model against prototype self heating tests, (ii) extending the framework to three dimensional building archetypes with plan irregularity and torsional response and to alternative damper layouts (for example, perimeter frames, corner braces, outrigger levels or partial storey coverage), (iii) exploring bridge applications in which FVDs already play a key role, and (iv) incorporating life cycle cost, ageing and maintenance metrics, and possibly semi active valve laws, into the objective set so that structural safety, device durability and economic performance can be optimised jointly

within a performance based design loop. A direct, one to one calibration of the present hydro thermal damper model against a new self heating test campaign for a specific prototype is therefore left to future work; here the constitutive choices and parameter windows are inherited from specimen scale experimental and CFD studies on civil FVDs [24, 61, 37, 60], and the focus is on how such a physically informed device behaves when it is optimised and embedded in a ten storey shear frame under strong ground motions.

Declaration of competing interest

The authors declare that they have no known competing financial interests or personal relationships that could have appeared to influence the work reported in this paper.

Appendix A. Supplementary symbols and derived quantities

Table A.1: Core structural and coupling symbols (definitions and SI units).

Symbol	Name	Units	Notes
$\boldsymbol{M}, \boldsymbol{C}_0, \boldsymbol{K}$	mass, damping, stiffness	kg; $\mathrm{N\,s\,m^{-1}}$; $\mathrm{N\,m^{-1}}$	See Eq. (1).
$\boldsymbol{x}, \boldsymbol{v}$	floor disp., vel.	m; $\mathrm{m\,s^{-1}}$	Relative to moving base.
$\boldsymbol{B}$	incidence matrix	–	Forms storey drifts.
$\boldsymbol{r}, a_g$	base vector, ground acc.	–; $\mathrm{m\,s^{-2}}$	Base term $-\boldsymbol{M}\boldsymbol{r}a_g$.
A_p, A_o $d_o, n_{\mathrm{orf}},$	piston, orifice area	$\mathrm{m^2}$	From $D_p, d_o, n_{\mathrm{orf}}$.
L_{ori}, D_p	orifice/piston geom.	m; –; m; m	Design vars; see Table 2.
$C_d^0, C_d^\infty, p_{\exp}$	discharge law params	–	In $C_d(\mathrm{Re})$.
Re	Reynolds number	–	$\mathrm{Re} = \rho|Q|d_o/(\mu A_o)$.
k_{sd}	elastic branch stiff.	$\mathrm{N\,m^{-1}}$	Hydraulic + spring stiffness.
$c_{\mathrm{lam}}(T)$	laminar coeff.	$\mathrm{N\,s\,m^{-1}}$	Equivalent viscous term.

Table A.2: Core damper and performance symbols (definitions and SI units).

Symbol	Name	Units	Notes
Δp_{kv}, Δp_{cav}, Δp_{eff}	jet, cavitation, eff. drop	Pa	Jet, cavitation and effective drop.
Q_{sat}, Q_{cap}	sat. flow, capacity	$\mathrm{m^3\,s^{-1}}$	Flow limit and capacity.
v_{ε}, $\varepsilon_{\mathrm{softmin}}$	smoothing params	$\mathrm{m\,s^{-1}}$; Pa	Velocity and soft-min smoothing.
T_o, T_s, hA	oil/steel T, conductance	°C; $\mathrm{W\,K^{-1}}$	Two-node thermal model.
$\mu(T)$, $\rho(T)$	viscosity, density	$\mathrm{Pa\,s}$; $\mathrm{kg\,m^{-3}}$	Temperature dependent.
PFA, IDR	PFA, IDR	$\mathrm{m\,s^{-2}}$; –	Main response metrics.
t_5, t_{95}	Arias window times	s	Define $[t_5, t_{95}]$.
P_{loss}, E_{mech}	power loss, energy	W; J	Loss and its time integral.

Table A.3: Structural model parameters for the 10-DOF shear frame benchmark, consistent with the 10-storey building used in [34, 43, 42].

Symbol	Name	Value	Units	Notes
n	storeys	10	–	One DOF per storey.
m_i	storey mass	3.60×10^5	kg	Uniform: $m_i = m$.
k_i	storey stiffness	6.50×10^8	N/m	Uniform: $k_i = k$.
c_i	damping coeff.	6.20×10^6	$\mathrm{N\,s\,m^{-1}}$	Uniform: $c_i = c$.
h	storey height	3.0	m	Used in Eq. (6).

Table A.4: Fixed numeric settings used in this study: optimization QC thresholds and ground-motion parameters.

Symbol	Value	Units	Notes
Optimization QC Thresholds (Section 3.1)			
$\Delta p_{95}^{\max}$	4.0×10^7	Pa	Per-record limit.
$(Q/Q_{\mathrm{cap}})_{95}^{\max}$	0.90	–	Max flow ratio.
$\mathrm{cav}^{\max}$	0.005	–	Max cavitation fraction (0.5%).
$T_{\mathrm{end}}^{\max}$	75	°C	Max oil temperature.
$\mu_{\mathrm{end}}^{\min}$	0.70	Pa s	Min end viscosity (Sec. 3.1).
Ground Motion Parameters (Section 2.4)			
hp_cut	0.05	Hz	High-pass cutoff.
band_fac	[0.8, 1.2]	–	Period band around T_1.
band_N	21	–	Number of periods.
s_bounds	[0.2, 2.2]	–	Scale factor range.

Table A.5: Fixed numeric settings used in this study: physical constants for the damper model.

Symbol	Value	Units	Notes
$p_{\mathrm{cav,eff}}$	2.0×10^3	Pa	Effective cavitation limit.
cav_sf	0.90	–	Cavitation safety factor.
v_ε	0.10	$\mathrm{m\,s^{-1}}$	Velocity smoothing scale.
$\varepsilon_{\mathrm{softmin}}$	1.0×10^6	Pa	Soft-min parameter.
$T_{\mathrm{ref}}, T_\infty$	25, 25	°C	Reference and ambient T.
ρ_{ref}	850	$\mathrm{kg\,m^{-3}}$	Reference density.
p_{amb}	1.0×10^5	Pa	Ambient pressure.
K_d	1.6×10^9	Pa	Effective bulk modulus.
L_{gap}	0.055	m	Gap length (k_h, k_s).
E_{body}	2.1×10^{11}	Pa	Cylinder modulus.
G_{sh}	7.9×10^{10}	Pa	Spring shear modulus.
b_μ	-0.013	$\mathrm{K^{-1}}$	Viscosity slope [45, 56].
α_ρ	9.2×10^{-4}	$\mathrm{K^{-1}}$	Density slope [56, 45].
Re_0	1000	–	Transition Re in $C_d(\mathrm{Re})$ [41, 5, 38].
b_ρ	4.5×10^{-7}	$\mathrm{K^{-2}}$	Quadratic density term [56].
C_o, C_s	*[derived]*	$\mathrm{J\,K^{-1}}$	Thermal capacitances.
c_p (oil)	1800	$\mathrm{J\,(kg\,K)^{-1}}$	Oil specific heat.
c_p (steel)	500	$\mathrm{J\,(kg\,K)^{-1}}$	Steel specific heat.

Table A.6: Derived quantities used internally (definitions).

Quantity	Definition	Notes
A_p	$\pi D_p^2/4$	Piston area (force $A_p \Delta p$).
A_o	$n_{\mathrm{orf}} \pi d_o^2/4$	Total orifice area.
R_{lam}	Eq. (14)	Laminar resistance.
k_h	$K_d A_p^2/L_{\mathrm{gap}}$	Hydraulic stiffness.
k_s	$E_{\mathrm{body}} A_p/L_{\mathrm{gap}}$	Cylinder stiffness.
k_{hyd}	$(1/k_h + 1/k_s)^{-1}$	Combined hydraulic stiffness.
k_p	$G_{\mathrm{sh}} d_w^4/(8 n_{\mathrm{turn}} D_m^3)$	Coil spring stiffness.
k_{sd}	$k_{\mathrm{hyd}} + k_p$	Elastic-branch stiffness.
L_h	$\rho L_{\mathrm{ori}}/A_o^2$	Hydraulic inertia.

References

[1] Abd, H.M., Alomar, O.R., Mohamed, I.A., 2019. Effects of varying orifice diameter and reynolds number on discharge coefficient and wall pressure. Flow Measurement and Instrumentation 65, 219–226. doi:`10.1016/j.flowmeasinst.2019.01.004`.

[2] Abdelrahman, A.M., Mobasher, A.M., 2021. Effect of varying orifice thickness on the discharge coefficient for different orifices shapes. ENGINEERING RESEARCH JOURNAL (ERJ) 1, 148–163.

[3] Acquaro, G., Postiglione, A., Pecora, G., D'Ambra, P., 2020. Comparative assessment of different typologies of fluid viscous dampers for seismic protection. Soil Dynamics and Earthquake Engineering 138, 106284. doi:`10.1016/j.soildyn.2020.106284`.

[4] Agha, M.E., Ras, A.A., Hamdaoui, K., 2023. Investigation of rheological and geometric properties effect on nonlinear behaviour of fluid viscous dampers. Journal of Applied Fluid Mechanics 16, 2142–2157. doi:`10.47176/jafm.16.11.1940`.

[5] Ahmed, E.N., Ghanem, A.A., 2020. A novel comprehensive correlation for discharge coefficient of square-edged concentric orifice plate at low reynolds numbers. Flow Measurement and Instrumentation 73. doi:`10.1016/j.flowmeasinst.2020.101751`.

[6] Akcelyan, S., Lignos, D.G., Hikino, T., 2018. Adaptive numerical method algorithms for nonlinear viscous and bilinear oil damper models subjected to dynamic loading. Soil Dynamics and Earthquake Engineering 113, 488–502. doi:`10.1016/j.soildyn.2018.06.021`.

[7] American Society of Civil Engineers, 2017. Minimum Design Loads and Associated Criteria for Buildings and Other Structures. asce/sei 7-16 ed. American Society of Civil Engineers. Reston, VA.

[8] Arjmand, M., Naderpour, H., Kheyroddin, A., 2024. Optimal control based on damage of concrete moment-resisting frames retrofitted with nonlinear viscous dampers. Structures 63. doi:`10.1016/j.istruc.2024.106387`.

[9] Bakhshinezhad, S., Mohebbi, M., 2020. Multi-objective optimal design of semi-active fluid viscous dampers for nonlinear structures using nsga-ii. Structures 24, 678–689. doi:10.1016/j.istruc.2020.02.004.

[10] Black, C.J., Makris, N., 2017. Viscous heating of fluid dampers under small and large amplitude motions: Experimental studies and parametric modeling. Journal of Engineering Mechanics doi:10.1061/ASCE0733-93992007133:5566.

[11] Cetin, H., Aydin, E., Ozturk, B., 2019. Optimal design and distribution of viscous dampers for shear building structures under seismic excitations. Frontiers in Built Environment 5. doi:10.3389/fbuil.2019.00090.

[12] Cheng, W., Shen, Y., Xu, G., 2020. Experimental and numerical modeling of sidewall orifices. SN Applied Sciences 2. doi:10.1007/s42452-020-2658-7.

[13] Cioncolini, A., Cassineri, S., Duff, J., Curioni, M., Scenini, F., 2018. Micro-orifice single-phase flow at very high reynolds number. Experimental Thermal and Fluid Science 91, 35–40. doi:10.1016/j.expthermflusci.2017.10.006.

[14] Crane Co., 1982. Flow of Fluids Through Valves, Fittings, and Pipe. Technical Paper 410M. Crane Co.. New York, N.Y. Metric Edition - SI Units (Fourth Printing).

[15] Cucuzza, R., Domaneschi, M., Greco, R., Marano, G.C., 2023. Numerical models comparison for fluid-viscous dampers: Performance investigations through genetic algorithm. Computers and Structures 288. doi:10.1016/j.compstruc.2023.107122.

[16] Cuturi, M., 2013. Sinkhorn distances: Lightspeed computation of optimal transport, in: Advances in Neural Information Processing Systems 26 (NeurIPS 2013), pp. 2292–2300.

[17] Davatgari-Tafreshi, M., Bora, S.S., 2023. Empirical ground-motion models (gmms) and associated correlations for cumulative absolute velocity, arias intensity, and significant durations calibrated on iranian strong motion database. Bulletin of Earthquake Engineering 21, 4139–4166. doi:10.1007/s10518-023-01708-9.

[18] Davoudi, M.R., Mahdi, M., 2021. Experimental and numerical investigation of geometric effect on cavitation flow through orifice. Mechanics and Industry 22. doi:10.1051/meca/2021018.

[19] Deringöl, A.H., Güneyisi, E.M., 2021. Influence of nonlinear fluid viscous dampers in controlling the seismic response of the base-isolated buildings. Structures 34, 1923–1941. doi:10.1016/j.istruc.2021.08.106.

[20] Domenico, D.D., Ricciardi, G., 2019. Earthquake protection of structures with nonlinear viscous dampers optimized through an energy-based stochastic approach. Engineering Structures 179, 523–539. doi:10.1016/j.engstruct.2018.09.076.

[21] Dong, B., Sause, R., Ricles, J.M., 2022. Modeling of nonlinear viscous damper response for analysis and design of earthquake-resistant building structures. Bulletin of Earthquake Engineering 20, 1841–1864. doi:10.1007/s10518-021-01306-7.

[22] Eiga, 2024. GUIDELINE FOR PRESSURE TESTING OF FIELD-INSTALLED PIPING AND EQUIPMENT. Technical Report. European Industrial Gases Association (EIGA). URL: www.eiga.eu.

[23] Farahpour, H., Hejazi, F., 2023. Development of adjustable fluid damper device for the bridges subjected to traffic loads. Structures 47, 1295–1322. doi:10.1016/j.istruc.2022.11.136.

[24] Frings, C., Zemp, R., De La Llera, J., 2017. MULTIPHYSICS MODELING, EXPERIMENTAL VALIDATION AND BUILDING IMPLEMENTATION OF VISCOUS FLUID DAMPERS, in: Proceedings of the 16th World Conference on Earthquake Engineering (16WCEE 2017), Santiago, Chile. pp. 1–11.

[25] Gao, J., Wu, F., 2019. Investigation of flow through the two-stage orifice. Engineering Applications of Computational Fluid Mechanics 13, 117–127. doi:10.1080/19942060.2018.1561517.

[26] Golijanek-Jędrzejczyk, A., Mrowiec, A., 2023. Cylindrical orifice testing in laminar flow with the orifice diameter ratio $\beta = 0.5$. Scientific Reports 13. doi:10.1038/s41598-023-42451-0.

[27] Groß, T.F., Pelz, P.F., 2017. Diffusion-driven nucleation from surface nuclei in hydrodynamic cavitation. Journal of Fluid Mechanics 830, 138–164. doi:10.1017/jfm.2017.587.

[28] Holschuh, B., Obropta, E., Newman, D., 2015. Low spring index niti coil actuators for use in active compression garments. IEEE/ASME Transactions on Mechatronics 20, 1264–1277. doi:10.1109/TMECH.2014.2328519.

[29] Hu, S., Hao, H., Meng, D., Yang, M., 2025. Theoretical and numerical study of the thermo-mechanical coupling effect on the fluid viscous damper. Journal of Sound and Vibration 597. doi:10.1016/j.jsv.2024.118846.

[30] Hutagalung, S.S., 2019. Effect of release coefficientof orifice plate on water fluid flow systems, in: Journal of Physics: Conference Series, Institute of Physics Publishing. p. 012086. doi:10.1088/1742-6596/1230/1/012086.

[31] Jankowski, T.A., Schmierer, E.N., Prenger, F.C., Ashworth, S.P., 2008. A series pressure drop representation for flow through orifice tubes. Journal of Fluids Engineering, Transactions of the ASME 130, 0512041–0512047. doi:10.1115/1.2907408.

[32] Jiang, Q., Zou, D., Liu, J., Qu, Y., Chen, K., Zhou, C., Li, D., 2025. Earthquake record truncation metric for nonlinear dynamic analyses of high rockfill dams. Structures 71. doi:10.1016/j.istruc.2024.107913.

[33] Kaleybar, R.S., Tehrani, P., 2021. Effects of using different arrangements and types of viscous dampers on seismic performance of intermediate steel moment frames in comparison with different passive dampers. Structures 33, 3382–3396. doi:10.1016/j.istruc.2021.06.079.

[34] Kayabekir, A.E., Bekdaş, G., Nigdeli, S.M., Geem, Z.W., 2020. Optimum design of PID controlled active tuned mass damper via modified harmony search. Applied Sciences 10, 2976. doi:10.3390/app10082976.

[35] Kolour, N.A., Basim, M.C., Chenaghlou, M., 2021a. Multi-objective optimum design of nonlinear viscous dampers in steel structures based on life cycle cost. Structures 34, 3776–3788. doi:10.1016/j.istruc.2021.09.100.

[36] Kolour, N.A., Basim, M.C., Chenaghlou, M., 2021b. Multi-objective optimum design of nonlinear viscous dampers in steel structures based on life cycle cost. STRUCTURES 34, 3776–3788. doi:10.1016/j.istruc.2021.09.100.

[37] Lak, H., Zahrai, S.M., 2023. Self-heating of viscous dampers under short- & long-duration loads: Experimental observations and numerical simulations. Structures 48, 275–287. doi:10.1016/j.istruc.2022.12.079.

[38] Lee, H.J., Choi, H., Jin, Y.I., Hwang, K.Y., Park, D.C., Min, S., 2018. Effect of nozzle inlet geometry in high temperature hydrocarbon liquid jets. International Journal of Heat and Fluid Flow 74, 1–14. doi:10.1016/j.ijheatfluidflow.2018.09.004.

[39] Liu, Y., Wang, J., Du, Y.F., Wu, J.H., 2023. Research on thermal effects of fluid viscous dampers considering damping force and viscosity–temperature characteristics. Applied Sciences 13. URL: https://www.mdpi.com/2076-3417/13/18/10358, doi:10.3390/app131810358.

[40] Michalczyk, K., Grzejda, R., Urbaś, A., Różyło, P., 2024. Effective computational model for determining the geometry of the transition zone of end coils of machined springs, enabling efficient use of the spring material. Materials 17. doi:10.3390/ma17071540.

[41] la Morena, D., Salvador, F.J., 2018. Experimental investigation of the effect of orifices. Fuel 213, 207–214.

[42] Ocak, A., Bekdaş, G., Nigdeli, S.M., Kim, S., Geem, Z.W., 2022a. Optimization of tuned liquid damper including different liquids for lateral displacement control of single and multi-story structures. Buildings 12, 377. doi:10.3390/buildings12030377.

[43] Ocak, A., Nigdeli, S.M., Bekdaş, G., Kim, S., Geem, Z.W., 2022b. Optimization of seismic base isolation system using adaptive harmony search algorithm. Sustainability 14, 7456. doi:10.3390/su14127456.

[44] Osman, H., Elsayed, K., Sedrak, M., 2019. Shape optimization of an orifice meter using the adjoint method and surrogate based optimization. Flow Measurement and Instrumentation 70. doi:10.1016/j.flowmeasinst.2019.101652.

[45] PM Tamson Instruments, 2019. Product information Silicon oil 200 10-100 cSt. Technical Report 200uk.doc (Rev 2.0). P.M. Tamson Instruments bv. Bleiswijk, The Netherlands.

[46] Ravelet, F., Danlos, A., Bakir, F., Croci, K., Khelladi, S., Sarraf, C., 2020. Development of attached cavitation at very low reynolds numbers from partial to super-cavitation. Applied Sciences 10, 7350. doi:`10.3390/app10207350`.

[47] Simpson, A., Ranade, V.V., 2018. Modelling of hydrodynamic cavitation with orifice: Influence of different orifice designs. Chemical Engineering Research and Design 136, 698–711. doi:`10.1016/j.cherd.2018.06.014`.

[48] Slovenski inštitut za standardizacijo, 2018. Anti-seismic devices. Slovenski Standard SIST EN 15129:2018. Slovenski inštitut za standardizacijo. Ljubljana, Slovenia. Identical to EN 15129:2018. Supersedes SIST EN 15129:2010.

[49] Song, Z., Lu, Y., 2016. Research and development of mechanically adjustable fluid viscous damper, in: Proceedings of the 2016 International Conference on Mechatronic Systems, Beijing, China. pp. 31–35. doi:`10.1109/ICMS.2016.7502120`.

[50] Swallow, F.E., 2002. Viscosity of polydimethylsiloxane gum: Shear and temperature dependence from dynamic and capillary rheometry. Journal of Applied Polymer Science 84, 2533–2540. doi:`10.1002/app.10563`.

[51] Tan, P.S., Farid, A.A., Karimzadeh, A., Koloor, S.S.R., Petrů, M., 2020. Investigation on the curvature correction factor of extension spring. Materials 13. doi:`10.3390/MA13184199`.

[52] Tang, L., Li, J., Xie, Y., Tian, Z., 2021. Experimental research on dynamic performance of viscous fluid damper, in: 2021 4th International Symposium on Traffic Transportation and Civil Architecture, ISTTCA 2021, Institute of Electrical and Electronics Engineers Inc.. pp. 437–440. doi:`10.1109/ISTTCA53489.2021.9654526`.

[53] Taylor Devices, Inc., 2024. Fluid viscous dampers: Seismic and shock isolation solutions. `https://www.taylordevices.com/products/fluid-viscous-dampers`. Erişim Tarihi: 12 Kasım 2025. (Üretici teknik föyü, 275 MPa (40 ksi) sızdırmazlık basınç kapasitesini belirtmektedir.).

[54] Vargas-Alzate, Y.F., Hurtado, J.E., Pujades, L.G., 2022. New insights into the relationship between seismic intensity measures and nonlinear structural response. Bulletin of Earthquake Engineering 20, 2329–2365. doi:10.1007/s10518-021-01283-x.

[55] Venczel, M., Bognár, G., Árpád Veress, 2021. Temperature-dependent viscosity model for silicone oil and its application in viscous dampers. Processes 9, 1–21. doi:10.3390/pr9020331.

[56] Wacker-Chemie GmbH, 2002. Wacker Silicone Fluids AK. Wacker-Chemie GmbH, Silicones Division. München, Germany. No. 4405e 1:02.

[57] Yau, K.H., Kua, E.C., Balvinder, S., 2017. Numerical investigation of a thick plate restriction orifice on the pressure drop performance, in: IOP Conference Series: Materials Science and Engineering, Institute of Physics Publishing. p. 012028. doi:10.1088/1757-899X/243/1/012028.

[58] Yetgin, A., Karakaş, A., Acar, B., Özaslan, E., 2024. Failure analysis of a helical compression spring with relatively low spring index. Engineering Failure Analysis 165. doi:10.1016/j.engfailanal.2024.108798.

[59] Zhai, S., Song, L., Lv, X., 2019. Measurement and analysis of silicone oil characteristics and viscosity-temperature index, in: IOP Conference Series: Earth and Environmental Science, Institute of Physics Publishing. p. 032049. doi:10.1088/1755-1315/330/3/032049.

[60] Zhang, Y., Xu, W., Wang, S., Du, D., Geng, Y., 2024. Mechanical modeling of viscous fluid damper with temperature and pressure coupling effects. Machines 12. doi:10.3390/machines12060366.

[61] Zhong, J., Wan, H.P., Yuan, W., He, M., Ren, W.X., 2020. Risk-informed sensitivity analysis and optimization of seismic mitigation strategy using gaussian process surrogate model. Soil Dynamics and Earthquake Engineering 138. doi:10.1016/j.soildyn.2020.106284.

[62] Zoccolini, L., Bruschi, E., Cattaneo, S., Quaglini, V., 2023. Current trends in fluid viscous dampers with semi-active and adaptive behavior. doi:10.3390/app131810358.